THE JOURNAL OF PHYSICAL CHEMISTRY C

Article

pubs.acs.org/JPCC

Defect Enhanced Efficient Physical Functionalization of Graphene with Gold Nanoparticles Probed by Resonance Raman Spectroscopy

Ravi K. Biroju[†] and P. K. Giri*[,†,‡]

[†]Centre for Nanotechnology and [‡]Department of Physics, Indian Institute of Technology Guwahati, Guwahati 781039, Assam, India

Supporting Information

ABSTRACT: We demonstrate efficient physical functionalization of single layer graphene with Au nanoparticles mediated by in-plane defects in graphene grown by a chemical vapor deposition technique. The effect of an ultrathin Au layer on the single layer, bi layer, and few layer graphene with intrinsic defects was studied by resonance Raman spectroscopy and high resolution transmission electron microscopy (HRTEM). We observed a striking enhancement in the intensity of sharp D and D′ bands after sputter deposition of an ultrathin Au layer on graphene. In contrast, G and 2D bands show a lower enhancement in intensity and a change in line width due to the charge transfer from Au to the graphene and strong interaction between the Au and graphene layers, respectively. X-ray photoelectron spectroscopy (XPS) analysis shows a 40% decrease in integrated intensity ratio of sp^3 and sp^2 bands in C-1s spectra after Au functionalization indicating bonding of Au atoms preferentially at the defect sites in graphene. This was further substantiated by HRTEM imaging and position dependent Raman spectral line shape analysis. The calculations of interdefect distance and areal defect density from the Raman analysis on the graphene−Au hybrid are in close agreement with the HRTEM analysis. Further, Raman spectral line shape dependence of Au functionalization on the number of layers in graphene reveals that Au functionalized single layer graphene behaves like a pristine bi layer graphene due to strong interaction between Au and the graphene layer. These results open up possibilities for efficient physical functionalization of graphene with foreign atoms through defect engineering for novel applications of graphene in catalysis, biosensors, and optoelectronic and photonic devices.

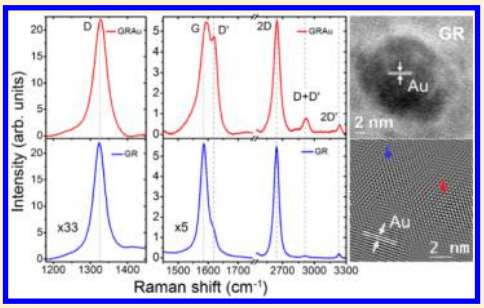

1. INTRODUCTION

Graphene, a two-dimensional (2D) prototype material, has revolutionized nanomaterials research[1] owing to its remarkable physical, chemical, mechanical, and electronic properties. The huge carrier mobility,[2] high optical transparency,[3] and high thermal conductivity[4] make it a unique material to explore the 2D physics for the fabrication of devices with a wide range of electronic and optoelectronics applications. Recently, graphene and graphene based hybrid nanoassemblies have gained considerable attention in optoelectronic devices such as displays, light-emitting diodes, and solar cells, which demands materials with low sheet resistivity and high transparency.[5−7] Graphene can fulfill multiple functions in light-conversion systems as the transparent conductive window, photoactive material, channel for charge transport, and catalyst.[7,8] For exploitation in electronics and photonics, graphene must be in close contact with other materials, which can change its electrical and optical properties. The substrate, charge impurities, doping with chemical functional groups, and metal contacts can shift the position of the Fermi level of graphene.[9,10] Graphene with plasmonic NPs offers a new perspective for light conversion systems by optimization of visible-light absorption via the surface plasmon resonance (SPR) of the NPs, followed by electron exchange between graphene and NPs and charge transport through graphene.[11]

Note that the interaction of foreign materials with pristine defect free graphene is very weak due to its inert nature of covalently bonded sp^2 carbon (C) atoms on the basal plane, as compared to chemically processed graphene having surface functionalities. It is generally believed that the covalent interface between graphene and noble metal starts from the defects such as nonhexagonal rings, vacancies, and oxygenated defect sites.[7] It is important to understand the possible approaches to enhance the interaction between metal and graphene with defect and defect free graphene for ensuing applications. While various point defects and line defects are unavoidable in chemical vapor deposition (CVD) grown graphene, its exploitation in the physical functionalization of graphene with noble metals has not been addressed in the literature.

Recent studies on graphene have focused on the interaction of transition metals with graphene in atomic scale, and various experimental tools have been exploited.[12−18] One of the important tools to probe the resonant effects between graphene and metal nanoparticles (NPs) is surface enhanced Raman spectroscopy (SERS). Significant Raman enhancements due to near field plasmonic effects in the vicinity of metal NPs and

Received: January 16, 2014
Revised: June 3, 2014
Published: June 4, 2014

   dx.doi.org/10.1021/jp500501e | J. Phys. Chem. C 2014, 118, 13833−13843

graphene were reported for different laser excitations.[19,20] Urich et al. reported the enhanced electron−phonon interaction by monitoring the SPR effect in the Ag−graphene hybrid structure.[13] Park et al. studied the Au NPs−graphene−Au film junction hybrid system to identify the layer breathing mode and other out-of-plane phonon modes of few layer graphene through SERS.[21] Very recently, we reported that graphene−metal hybrids play a crucial role in the controlled fabrication of 1D semiconducting nanorod (NR) and nanowire (NW) heterostructures with improved optoelectronic properties.[22] To date, to our knowledge, only one report[7] has addressed the issue of the noble metal interaction with defective graphene. However, there is a lack of in-depth understanding on the role of defects in the interactions between graphene and foreign atoms and molecules. It is anticipated that a proper understanding on the interaction of noble metal with defective graphene would pave the way for controlled functionalization of graphene for cutting edge applications.

In this work, we present a systematic investigation on the interaction of Au nanoparticles (NPs) with in-plane defects in graphene by using micro-Raman spectroscopy and high resolution transmission electron microscopy (HRTEM) analyses. Interestingly, we found significant changes in the characteristic D, G, and 2D Raman modes in graphene due to attachment of Au NPs at the defect sites in graphene without altering the sp^2 crystalline nature of graphene. Evolution of G and 2D bands is correlated with the change in the binding energy of C atoms and full width at half-maximum (fwhm) of the sp^2 and sp^3 bands along with decrease of the sp^3 to sp^2 integrated intensity ratio of the C-1s core level spectrum in XPS. In the presence of defects, we find strongly enhanced interaction of foreign atoms (transition metals) with graphene, which to the best of our knowledge has not been reported earlier by means of a physical approach. We compare the results with other noble metals (e.g., Cu) and organic semiconductors (e.g, CoPc) and elucidate the crucial role of defects in the enhanced interaction of Au NPs with graphene, leading to efficient physical functionalization of graphene at room temperature.

2. EXPERIMENTAL SECTION

2.1. Synthesis of Graphene. We synthesized monolayer and few layer graphene by using a catalytic chemical vapor deposition (CVD) system on a Cu foil of thickness 25 μm (Alfa-Aesar). First, the Cu foil was inserted into a quartz chamber and flushed with argon gas for 5 min. Then, the chamber was pumped to base vacuum 4×10^{-4} mbar and the temperature was increased to 1000 °C (growth temperature of graphene) at a rate of 25 °C min^{-1} using a horizontal muffle furnace (Indfur, India). Substrate was pre-annealed at the same temperature, in reduced environment by flowing 200 sccm (standard cubic centimeters per minute) H_2 gas for 30 min in order to avoid oxidation of the Cu surface. The final reaction was carried out by controlled flow of CH_4 ∼18 sccm and H_2 ∼200 sccm for 30 min at a temperature of 1000 °C and a pressure of 4.0 mbar. Since graphene was deposited on both sides of the Cu foil, the bottom layer was removed by diamond polishing. The graphene layer on top of the Cu foil was transferred onto Si/SiO_2 substrate by a conventional wet transfer technique.[23] In this process, poly(methyl methacrylate) (PMMA)/toluene was spin coated on the graphene/Cu and the underlying Cu was etched in an aqueous $Fe(NO_3)_3$ etchant solution. PMMA/graphene floating on the etchant solution was rinsed in deionized water for a few times, until the PMMA and metal impurities were removed. Then, it was scooped and transferred onto Si/SiO_2 and quartz substrates.

2.2. H_2 Annealing of Graphene. Achieving high quality graphene without wrinkles, folds, and surface corrugation is one of the challenging tasks while transferring it from Cu foil to a required substrate. Though wet transfer is a standard protocol, there are still leftover impurities such as PMMA and catalyst NPs along with the oxide traces that are present on the graphene substrate. In order to remove these impurities from the graphene on Si/SiO_2 and TEM grid, these samples were annealed in H_2 atmosphere. Initially, the samples were taken in a quartz boat and kept in the tubular chamber. Initially, the chamber was pumped up to a base vacuum of 10^{-5} mbar followed by ramping of the temperature up to 400 °C. The graphene annealing was performed under H_2 gas environment for 2 h. The annealing parameters were chosen optimum to achieve a clean graphene without the residual impurities on the graphene surface.[24] The degree of improvement in the crystallinity and spatial homogeneity of graphene layers were confirmed by Raman spectra and Raman mapping in each case before and after annealing, respectively (see the Supporting Information, Figure S1). These samples are further studied for the physical functionalization with metal and organic molecules.

2.3. Surface Functionalization of Graphene by Au. In the next step, ultrathin Au film was deposited on the graphene layer by a radio frequency (RF) magnetron sputtering process under an Ar gas atmosphere with a RF power of <5 W. Au film was deposited in a controlled way for 30 s at a deposition rate of 0.8 Å/s. For comparison, Au film was deposited on the Si/SiO_2/graphene substrate and graphene transferred onto the TEM Cu grid. For the convenience of discussion, we have denoted the pristine graphene samples as GR and the Au coated graphene sample as GRAu. For comparison, an ultrathin Cu film (∼2 nm) was deposited on another graphene sample by a DC sputtering method under an Ar gas atmosphere in the same chamber. A high purity Cu disc (99.99%, Alfa-Aesar) was used as the target material for the sputter deposition.

2.4. Characterizations. Micro Raman measurements were performed with a high resolution spectrometer (Horiba LabRam HR), with excitation wavelengths (λ_{ex}) of 488 and 514.5 nm (Ar^+ ion laser) and 632.8 nm (He−Ne laser). The excitation source was focused with a 100× objective lens, a spot size of 2 μm, and a laser power of 1 mW to avoid heating and damage to the sample, and the signal was collected by a CCD in a back scattering geometry sent through a multimode fiber grating of 1800 grooves/mm. Raman mapping was carried out in the 10×10 μm^2 frame size on the samples at 514.5 nm laser excitation. Scanning electron microscopy (SEM) was performed by standard SEM (LEO 1430VP), field emission SEM (FESEM) (Sigma, Zeiss, operating voltage 0.5−30 kV) imaging using an in-lens detector, and HRTEM (JEOL-2100 operated at 200 kV). X-ray photoelectron spectroscopy (XPS) measurements were carried out with a fully automated XPS microprobe (PHI-Xtool, Ulvac-Phi) using an Al Kα X-ray beam (1486.7 eV). The standard carbon 1s spectrum was used for the calibration of the XPS spectra recorded for various samples. Atomic force microscopy (AFM) imaging was done by a scanning probe microscope (5500, Agilent Technologies).

2.5. Spectral Data Analysis. Line shape analysis refers to the extraction of the center, full width at half-maximum (fwhm), and intensity of a peak by fitting. Raman spectral lines of GR and GRAu were fitted by Lorentzian line shapes, and

XPS line shape analysis was performed by Gaussian peak fitting using a Peakfit software with peak parameters as free variables. The best fit was obtained by a large number of iterations.

3. RESULTS AND DISCUSSION

3.1. Raman Analysis of Pristine Graphene. The crystalline nature and number of layers in CVD synthesized graphene were probed primarily by Raman spectroscopy. Figure 1a shows a set of typical Raman spectra of as-grown graphene at an excitation wavelength (λ_{ex}) of 514.5 nm corresponding to scanning positions marked by the serial numbers shown in the optical microscope (OM) image of Figure 1b. The strong Raman feature observed at 1590 cm^{-1} is the E_{2g} mode (G band), assigned for the in-plane stretching of C−C bonds, which dictates the graphitic sp^2 crystalline nature of the carbon. The Raman mode at 2700 cm^{-1} (a fingerprint of graphene, known as the G′ or 2D band) originates from the second order double resonance process related to a phonon near the K point in graphene. The line shape of the 2D band is very sensitive to the number of layers. The Raman feature at 1352 cm^{-1}, known as the D band, arises from breathing of the hexagonal carbon ring due to the presence of defects. This mode originates from the transverse optical (TO) phonon due to the intervalley double resonance process at the Brillouin zone corner K, such as vacancies or grain boundaries, and substitutional heteroatoms.[25,26] A small shoulder at the higher frequency side of the G band (~1630 cm^{-1}) arises from the intravalley double resonance process at the K point and is called the D′ band. The D′ band mainly originates from structural disorder or edges in graphene.[27] Raman data acquired at several spots on graphene show similar Raman features. These collective Raman spectra revealed the coverage of large area single layer graphene (SLG) and bi layer graphene (BLG) in the as-grown GR sample, as revealed from the Raman line shape analysis of the 2D band. Note that no apparent shift in G band was observed for spectra taken at different spots, indicating uniformity of the as-grown graphene layer.[28] However, a marginal shift in the position of the 2D band for different spots may be due to local nonuniformity/wrinkles in the layer while transferring from the Cu substrate to the SiO_2 substrate. Graphene annealing was performed in order to remove the charge impurities coming from the PMMA and Cu catalyst NPs. The crystalline quality of as transferred graphene was improved by the graphene annealing described in section 2.2. Raman spectra of cleaned graphene before and after annealing are shown in Figure S1 (Supporting Information). The crystalline nature of the GR was further investigated by TEM imaging. Figure 1c shows a low resolution TEM image of the graphene layer, and the inset represents the corresponding selected area electron diffraction (SAED) pattern, which confirms the hexagonal diffraction patterns of the single crystalline graphene layer.

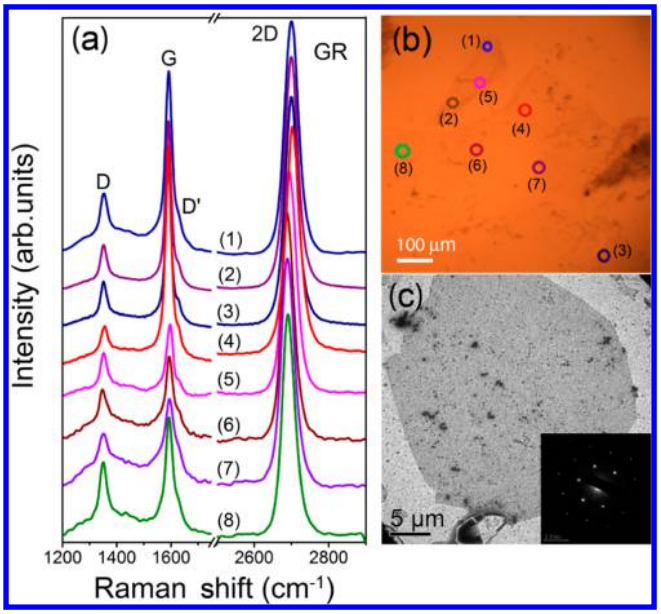

Figure 1. (a) Characteristic Raman features of as-grown graphene transferred onto Si/SiO_2 substrate and (b) corresponding OM image showing the scanned area for each spectra marked with a serial number. These spectra were recorded with 514.5 nm excitation. (c) Low resolution TEM image of a graphene layer transferred onto a TEM grid; the inset shows the corresponding diffraction pattern of the hexagonal single crystal sp^2 carbon atoms.

Further, the resonant Raman features of the graphene were probed by λ_{ex} = 632.8 nm, which show strongly enahanced intensity of the Raman modes as compared to that found with 514.5 nm excitation. Figure 2a and b depicts the Lorentzian line shapes (fitted lines shown with blue color) of key Raman features in single (SLG) and bi layer graphene (BLG) that show a substantial amount of defects characterized by the distinct D and D′ bands. Line shape analysis of the 2D band shows that 90% of the substrate is covered by SLG which was further supported by the Raman mapping presented later. As

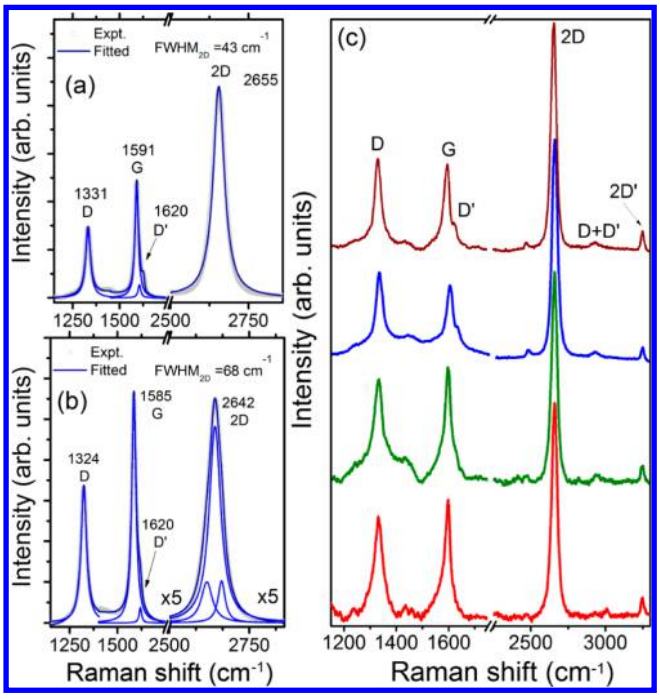

Figure 2. Raman spectra recorded with an excitation wavelength of 632.8 nm for (a) single layer and (b) bi layer graphene; the experimental data are fitted with Lorentzian line shapes. Standard peaks are marked with the peak position in cm^{-1} units. The spectrum in part b is scaled up by a factor of 5 to enable comparison with part a. (c) Raman features of single layer graphene at different locations of the same sample, showing nearly equal intensities of sharp G and D bands. This implies the presence of point/extended defects on the graphene basal plane and imperfect edges.

dx.doi.org/10.1021/jp500501e | J. Phys. Chem. C 2014, 118, 13833−13843

evident from the resonant Raman spectra of Figure 2a and b, the intensity of the sharp D band is nearly half the intensity of the G band (I_D/I_G = 0.6) and the D′ band is relatively weak. This implies the presence of vacancy type defects on the basal plane of graphene including reconstructive defects at the edges that are formed during the growth process.[27] In addition, we observed equal intensities of the D and G bands with fwhm ~31 cm^{-1} at some portions on the graphene layer. Usually, D and G bands with a large fwhm (>80 cm^{-1}) arise for a large amount of sp^3 carbon. Such features were not observed in our CVD grown graphene, though it has been observed in the case of chemically prepared graphene sheets and ion bombarded graphene samples.[29] In the case of chemical processing, the surface functional groups such as hydroxyls and epoxides are present on the basal plane of the graphene, though it shows perfectly sp^2 crystalline nature (see the Supporting Information, Figure S2). These functional groups help to bind the metal NPs.[7,30] In our CVD graphene sample, the fwhm of both D ($\Delta\omega_D$) and G ($\Delta\omega_G$) bands is ~30−40 cm^{-1} and it implies the presence of point defects and extended defects on the basal plane of the graphene without losing its sp^2 crystalline nature.[27] This is consistent with the corresponding sharp 2D band. Note that the 2D band in SLG shows a fwhm of 43 cm^{-1}, while that in BLG shows a fwhm of 68 cm^{-1}.

Figure 2c represents a set of Raman spectra for defective graphene at different positions where the intensities of the D and G bands were found to be nearly equal, implying significant presence of in-plane defects such as mono, bi, and multiple vacancies.[27] These defects play a crucial role in the interaction of Au NPs with the graphene layer. For example, the defects may play an important role in the adsorption of metal species on graphene that enhance the catalytic activity of metal−graphene hybrid structures.[31,32] Electron microscopy and DFT calculations have revealed that metal atoms are attracted by the reconstructed defects bonded with an energy of 2 eV[33] and adsorption energy increases with the number of surface defects. However, this leads to heavy lattice distortions of the starting structure due to the formation of chemical bonds between the metal atoms and defects.[34] Thus, a controlled amount of in-plane defects is crucial for controlled functionalization of graphene with desired properties without losing the sp^2 character of the resulting structure. In the present case, an appropriate amount of defects is formed on the graphene layer during the CVD growth as discussed below.

3.2. HRTEM Imaging of GR and GRAu. Figure 3a shows the HRTEM image of the as grown graphene layer showing SLG and BLG. The arrow marks indicate the wrinkles (dark contrast regions) and edge of the graphene layer. Inset II shows a magnified view of region I in Figure 3a, which depicts the honeycomb hexagonal lattice of carbon atoms on the graphene plane. Figure 3b illustrates various kinds of defects in the same GR sample indicated by different colored arrows: green, edge imperfections; red, line defects; pink, vacancies and corresponding SAED pattern. A schematic of typical point and extended defects on the graphene layer, such as single, bi, multiple vacancies, line defects, and edge reconstruction, as modeled by ATK 11.8.2, (Quantumwise), is shown in Figure 3c. Such defects are inevitably present in our CVD grown graphene samples. Figure 3d illustrates the HRTEM images of the GRAu hybrid grown on a TEM Cu grid. It indicates that the Au NPs are present at the defect sites of graphene, more prominently at the edges. Raman analysis shows that the as synthesized graphene contains a large number of defects on the

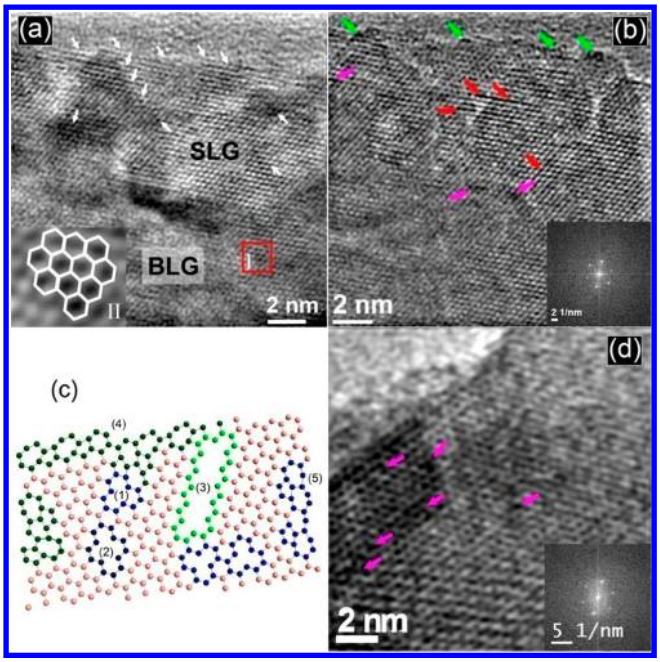

Figure 3. (a) HRTEM image of SLG and BLG. The white arrows indicate wrinkles and edge on SLG. The contrast difference in the image is due to the wrinkles of the graphene layer. Inset II is a magnified image of region of I. (b) HRTEM image of graphene with the corresponding SAED pattern in the inset; various colored arrows indicate the presence of different kinds of defects (green, edge defects; red, line defects; pink, vacancies). (c) Schematic of the molecular model of a graphene sheet with various defects, such as (1) single vacancy, (2) bi vacancies, (3) line defects, (4) zigzag, and (5) arm chair edge reconstructions highlighted by colored carbon atoms on the basal plane, which was modeled by the ATK simulation tool (Quantumwise, 11.8.2 version). (d) HRTEM image of GRAu showing the additional vacancy defects (pink arrows) after Au deposition; the corresponding SAED pattern is shown as an inset.

basal plane and imperfect edges, as evident from the D′ band in the pristine graphene. After Au deposition, it was found that the Au islands were formed not only at the edges (see Figure 3d) but also at the defect sites on the basal plane of graphene. These features are extensively probed by HRTEM imaging and Raman analysis. FESEM and TEM images of the surface morphology of GR and GRAu are presented in Figure S3 (Supporting Information). In the case of Au coated graphene, the size of Au NPs varies in the range 5−10 nm with oval shape (Figure S2d, Supporting Information). The Au NPs are shown with blue arrows in the figure. A careful look at the lattice image of Figure 3d reveals a considerable increase in vacancy defects after Au functionalization of GR (indicated by pink colored arrows). Interestingly, we observed a major enhancement in the intensity of D and D′ bands after Au deposition, as compared to that of G and 2D bands, as discussed next.

3.3. Raman Analysis of GRAu. It is well-known that, except for the G band, all second order double resonance Raman modes D, D′, 2D, D+D′, and 2D′ including weak combinational modes between 1700 and 2300 cm^{-1} of graphene are strongly dispersive in nature with respect to λ_{ex}.[35,36] We have carried out Raman studies on GR and GRAu with λ_{ex} = 632.8 nm, as strong resonance Raman features were observed in the GR sample at this wavelength. Figure 4a and b depicts the comparison of Raman features of GR and GRAu, and Figure 4c shows an enlarged view of the enhanced second

dx.doi.org/10.1021/jp500501e | J. Phys. Chem. C 2014, 118, 13833−13843

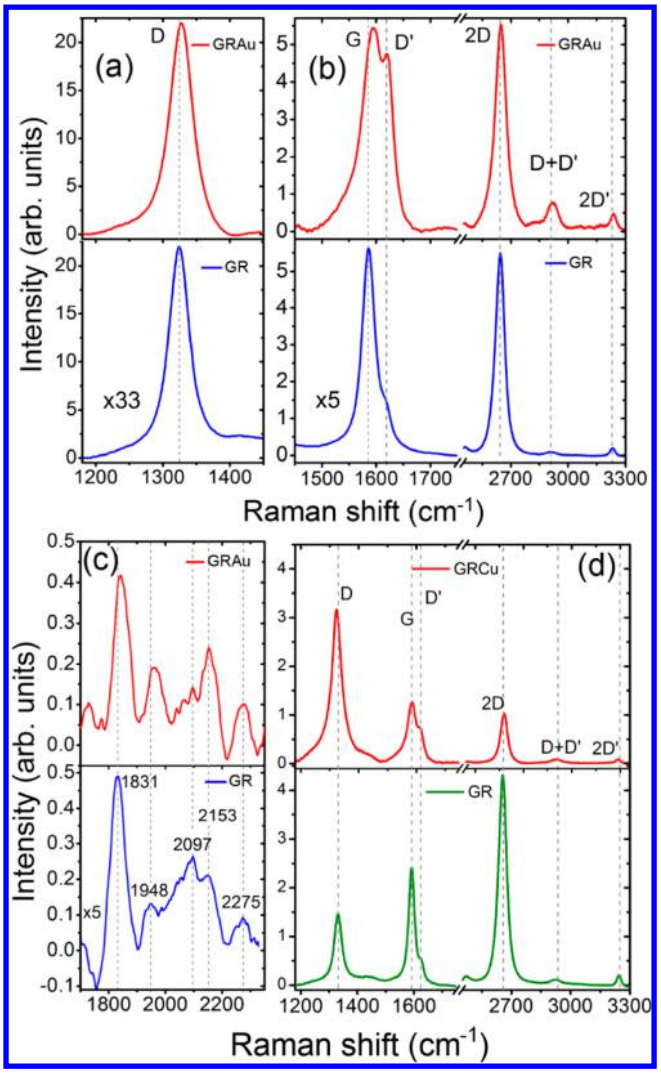

Figure 4. Comparison of the Raman spectra of graphene before and after Au deposition (blue and red lines): (a) D band; (b) G, D′, 2D, D +D′, and 2D′ bands. Note the respective scaling factors in each data set. (c) Comparison of the second order double resonance weak Raman modes in the range 1700−2300 cm^{-1} (scaled up by a factor of 5) in the GR and GRAu samples. (d) Comparison of the Raman spectra of the GR and GRCu samples.

order double resonance weak Raman modes after Au deposition on GR. For the GR sample, the data shown for the D band in Figure 4a is scaled up by a factor of 33 and the G and 2D bands are scaled up by a factor of 5 (blue curve) to enable comparison of all the features before and after Au deposition. It may be noted that no substantial change in the fwhm and position of the D and D′ bands was observed after Au deposition. It is clear that, in GRAu, the D band intensity is enhanced by a factor of ∼33, while the D′ band is enhanced by a factor of ∼13 as compared to that of GR. In contrast, the intensity of G, 2D, D+D′, and 2D′ bands is increased by a factor of ∼5 only in GRAu. Interestingly, the second order weak modes are equally enhanced in GRAu. In addition, it is found that the fwhm of the 2D band ($\Delta\omega_{2D}$) in GRAu is significantly higher (70 cm^{-1}) than that in GR (43 cm^{-1}). Note that the fwhm of 2D in pristine BLG was similar to that of the Au coated SLG (GRAu). Since fwhm is a measure of the number of layers in graphene, this would imply that, with an ultrathin Au layer on SLG, it behaves like a pristine BLG, where interaction between the layers is significant. In addition, the higher fwhm in GRAu may be partly caused by the diffusion of Au into the graphene layer due to the presence of defects.

In order to understand the different level of enhancement of different Raman bands and specific role of Au NPs in the Raman enhancement, we performed functionalization of graphene with another noble metal, Cu, and an organic semiconductor, cobalt pthalocyanine (CoPc) thin film (∼5 nm), deposited by DC sputtering and thermal evaporation, respectively. Figure 4d illustrates the comparative Raman features of GR and Cu coated GR (GRCu) samples. In the case of GRCu, the D band intensity is enhanced only by a factor of ∼2, while that of the G and 2D bands is reduced by a factor of 2 and 4, respectively. Further, $\Delta\omega_{2D}$ is almost identical in both GR (43 cm^{-1}) and GRCu (44 cm^{-1}), which is in contrast to the higher $\Delta\omega_{2D}$ (70 cm^{-1}) in GRAu. In the case of CoPc coating on GR, D, G, and D′ bands are marginally enhanced only by a factor of 1.5, while the 2D band is reduced to 0.6 of the original value (Supporting Information, Figure S4). Thus, the GRAu system shows very high enhancement in both D and D′ bands as compared to the cases of GRCu and GRCoPc.

The Raman enhancement may have two contributions, one caused by the SPR of Au NPs in the vicinity of defects in graphene and the other due to the enhanced defect density in GRAu as compared to that of GR. As compared to the Au induced enhancement in G and 2D bands, stronger enhancement in D and D′ bands suggests preferential clustering of Au NPs at the defect sites and a SPR enhancement effect in the Raman spectra. Since the Au NPs are well-known for their high SPR effects as compared to the Cu NPs, our results are fully consistent with the hypothesis that Au NPs preferentially migrate to the defect sites in GR. In order to support the resonance Raman effect, we have performed the absorption measurements of GR, GRAu, and GRCu hybrids fabricated on the quartz substrates. Figure S5 (Supporting Information) shows the absorption spectra of GR, GRAu, and GRCu on a quartz substrate. Au NP and Cu NP SPR peaks were found at 570 and 445 nm, respectively. The key points identified from this data are the stronger SPR absorption peak in GRAu than that of GRCu. Further, the SPR absorption peak of GRAu is stronger by a factor of 2 with respect to the AuNPs alone and a redshift, which may be due to the covalent functionalization of Au with defective graphene. The size and shape of the Au NPs decide the amount of SPR enhancement. Due to the small size of the Au NPs formed here limited by the thickness of the Au layer, SPR enhancement was only about 1 order of magnitude. Change in the defect density can be calculated from the intensity ratio of the D band to the G band (I_D/I_G), as discussed later. Note that the SPR absorption induced reduction in Raman intensity is insignificant here, since the surface coverage of the Au NPs on the graphene is much smaller than the maximum possible coverage.[8] In the case of CoPc on graphene, SPR enhancement is less, as expected from its dielectric behavior. Despite the absorption loss in the CoPc layer, marginal SPR enhancement was observed in this case. One may expect aggregation and bonding of the respective atoms/molecules covalently at the defect sites of graphene. The strongly enhanced D and D′ bands in the GRAu spectrum thus confirm the strong interaction of Au NPs at the in-plane defects and edges. Our results are in contradistinction to the conclusion of Wang et al.[20] who attributed the enhanced D and D′ bands in the Au coated graphene layer entirely to

dx.doi.org/10.1021/jp500501e | J. Phys. Chem. C 2014, 118, 13833−13843

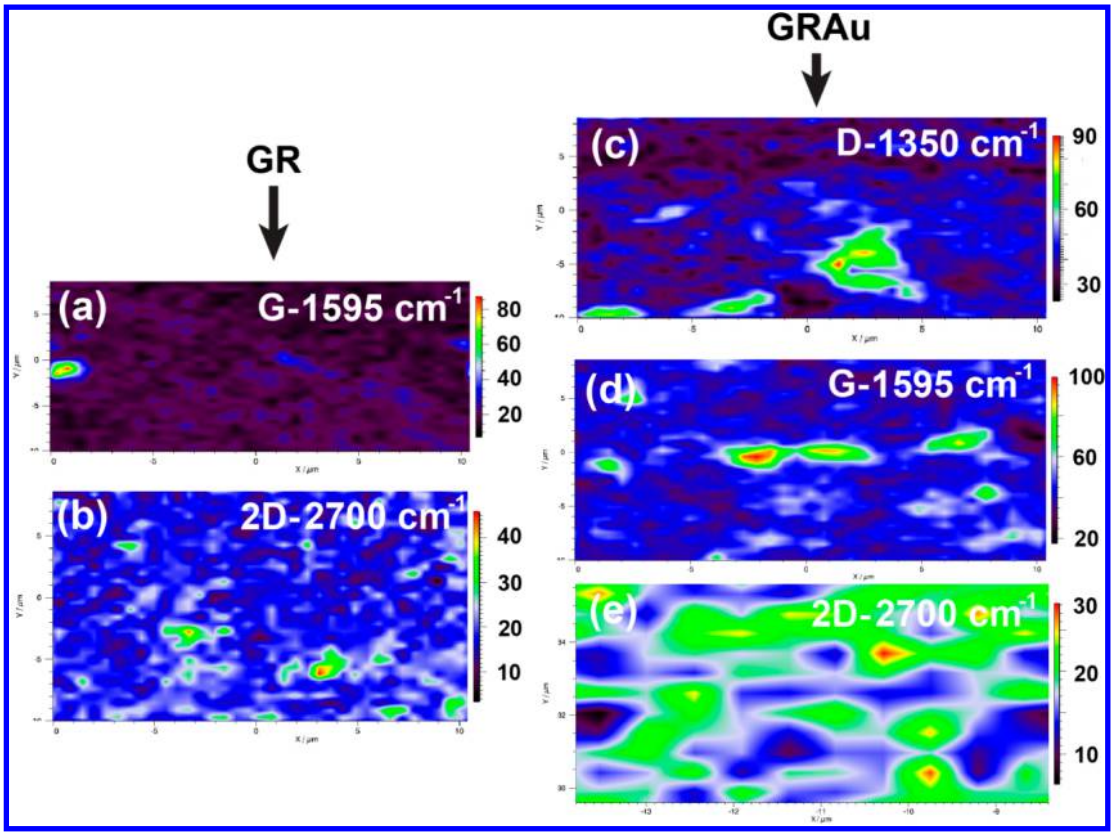

Figure 5. Raman maps of (a, b) GR and (c–e) GRAu samples showing D (1350 cm^{-1}), G (1595 cm^{-1}), and 2D (2700 cm^{-1}) bands with 514.5 nm laser excitation. Note that each band is scanned in the same area of 10 × 10 μm^2 and the intensity bar is drawn in the right for clarity.

increase in defect density caused by the Au adatoms, without considering the SPR effect. Ding et al. reported a decrease in intensity of the radial breathing mode and G band in the metal–single walled carbon nanotube (SWCNT) interface, and it was correlated with the transfer of electron from SWCNT to the Au NPs.[7]

Au NP induced charge transfer from Au to graphene was reported[8] on the basis of the downshift in the G and 2D bands. In our experiment, no reduction in the intensities of G and 2D bands was found on Au coated GR. However, SPR induced Raman intensity enhancement was less in the G and 2D bands as compared to the D band. Further, we noticed a small upshift (~3 cm^{-1}) in the 2D band and relatively large upshift in the G band after Au functionalization of graphene. This is indicative of the hole doping of the graphene layer[8] caused by the Au NPs attached at the defect sites. Besides the SPR enhancement in D, D′, and G bands due to functionalization with Au NPs, a significant enhancement in second order weak modes in the range 1700–2300 cm^{-1} was also observed, as shown in Figure 4c. In particular, the mode at 1948 cm^{-1} becomes stronger after Au functionalization. The stronger second order modes may be partly due to the SPR enhancement and partly due to adatom induced defects/disorder as well as the interlayer interactions.[35] The exact origin of these second order weak modes is not understood in the literature, though it has been attributed to combination modes by some groups. It is likely that some of these modes may be caused by the defects/disorder induced by the incorporation of the Au NPs in GR. In the presence of defects, the k-selection rule is relaxed and thus some of the forbidden modes may become Raman allowed modes in the defective GR.

3.4. Raman Mapping. Figure 5 illustrates the areal intensity maps of characteristic Raman modes of graphene before and after Au deposition in the scanning area 10 × 10 μm^2. Note that the intensity scale bars are separately shown for better visibility of each band. Figure 5a and b shows the relative areal intensity maps of the G and 2D bands, which is evidence for the large coverage of SLG and BLG in the graphene layer. Figure 5c–e depicts the Au coverage on GR substrate, which is shown by the intensity variations of the D, G, and 2D bands. A higher intensity of the D band compared to the 2D band reveals that the Au NPs are embedded at defect sites on the SLG and BLG.

3.5. HRTEM Analysis. The HRTEM images of GRAu at the graphene edge and in-plane defect sites with corresponding SAED patterns are shown in parts a and b of Figure 6, respectively. Parts c and d of Figure 6 show the inverse fast Fourier transform (IFFT) images of regions I and II marked in parts a and b of Figure 6, which depict the interface of the Au cluster at the graphene imperfect edge and in-plane defect sites, respectively. Lattice fringes of both Au and graphene are clearly discernible in the IFFT images (Figure 6c and d). Blue and red colored arrows indicate the lattice fringes of SLG and BLG in the GRAu sample, respectively. The bright and dark contrast portions in Figure 6c arise due to the wrinkles present on the basal plane of graphene.

The distribution of Au NPs on the graphene layers is further probed by HRTEM imaging, as shown in Figure 7a. The sample was obtained with direct deposition of Au on graphene transferred onto a TEM grid. Bright and dark contrast regions represent the lattice patterns of the graphene without and with Au NPs located by blue colored arrows and white marked ovals,

dx.doi.org/10.1021/jp500501e | J. Phys. Chem. C 2014, 118, 13833–13843

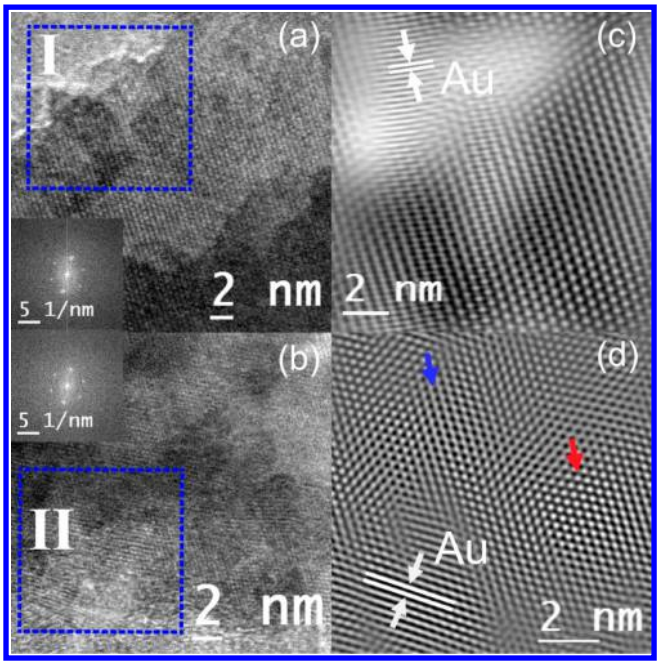

Figure 6. HRTEM lattice images of the GRAu hybrid: (a) Au NPs at the graphene edge and (b) Au NPs at the in-plane defects in the graphene basal plane. The corresponding FFT patterns are shown as an inset in each case. (c, d) IFFT images of regions I and II shown in parts a and b, which depict the lattice fringes of both graphene and Au NPs side by side. Blue and red arrows in part d indicate the single and bi layer graphene lattice fringes.

respectively. The white markers indicate the typical distance between centers of two Au NPs, which are ∼5 nm (a) and ∼9 nm (b). The analyses done over the several Au NPs shown in the HRTEM image reveal an average distance of ∼7 nm. Presuming that the Au NPs are present only at the defect sites, the average distance between the nearest-neighbor defect sites would be the same as above. Interestingly, the interdefect distance calculated from the Raman analysis (discussed later) is found to be in excellent agreement with the above HRTEM analysis. The defect mediated embedding of Au NPs with a size of 10 nm in graphene is depicted in Figure 7b. The lattice fringes of Au are clearly seen in the image. The effect of Au clustering on the graphene layer is shown further by the IFFT image in Figure 7c, which corresponds to region I in Figure 7b. This image reveals covalent functionalization of graphene with Au by displaying clear lattice fringes of both Au and graphene side by side. Blue and red colored arrows indicate the lattice patterns and atomic distortions due to the Au−C bonding originated from the defect sites on the basal plane of the graphene lattice.

3.6. AFM Analysis of GRAu. AFM topography was carried out to monitor the distribution of Au NPs at the defect sites in graphene. Parts a and b of Figure 8 represent the topography images of GRAu at the planar site (with in-plane defects) and edges, respectively. The Au islands at the edges and in-plane defect sites are represented by dark blue and dark green arrows, respectively. Comparison of Figure 8a and b reveals that the density of Au NPs is higher at the edge than that at the basal plane of graphene. Our results are consistent with the atomic resolution transmission electron microscopy (TEM) imaging and DFT simulations reported by Wang et al.[37] It was argued that, due to high binding energies of metal atoms to graphene edges, atomic chains can be formed by self-assembly of metal

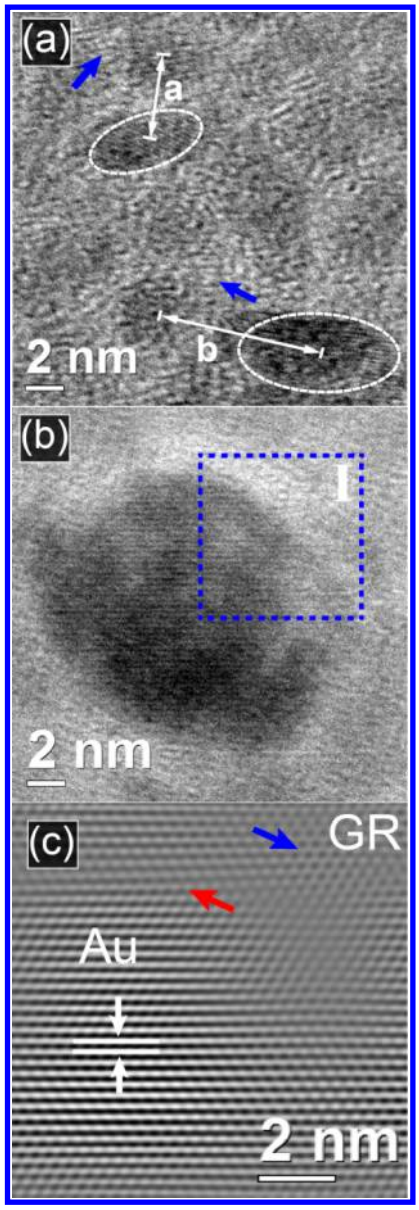

Figure 7. HRTEM lattice image of GRAu placed onto a TEM grid: (a) Au NPs (size ∼5−10 nm) located at the in-plane defects in graphene. Lattice fringes of both graphene and Au NPs are indicated by blue arrows and white marked oval regions (bright and dark contrast regions), respectively. The white colored marker lines indicate the distance (a = 5 nm, b = 9 nm) between two consecutive Au NPs. (b) Magnified lattice image of GR and Au shown in part a indicating covalent attachment of Au NPs (∼10 nm) with the graphene lattice. (c) IFFT image of the marked region I shown in part b, showing the lattice fringes of both the graphene (blue arrow) and Au cluster. The red colored arrow shows the lattice distortion on the graphene basal plane due to Au−C bonding.

atoms on the zigzag edge. Through DFT calculation, it was predicted that single metal atoms are preferentially located in the valleys of a zigzag edge of graphene. Figure 8a also reveals that the size of the Au NPs varied spatially to some extent owing to the nonuniform density (areal) of defects in graphene; i.e., bigger Au NPs correspond to sites for bigger size vacancies and vice versa. This is fully consistent with the position dependent Raman analysis, discussed later. In particular, our experiments lend strong support to the theoretical prediction that defect sites in graphene with higher surface energy are

dx.doi.org/10.1021/jp500501e | J. Phys. Chem. C 2014, 118, 13833−13843

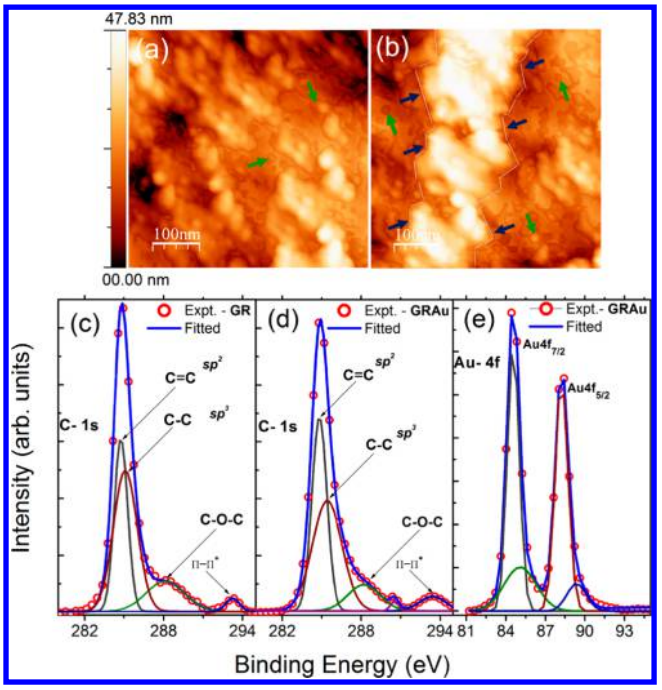

Figure 8. AFM topography images of GRAu: (a) Au NPs shown by dark green arrows at the defect sites on the basal plane and (b) Au NPs at the edges shown by dark blue arrows. Core level XPS spectra: (c) C-1s of GR, (d) C-1s of GRAu, and (e) Au-4f of GRAu, fitted with Gaussian line shape in each case. Contributions from different species are labeled in each case.

more favorable sites for functionalization with Au compared to the defect free sites in graphene.[34] These results demonstrate that the defects in graphene strongly enhance the interaction of foreign atoms with graphene. Recently, we have demonstrated the application of graphene–Au hybrid in the growth of highly aligned ZnO NRs and NWs on rapid thermally annealed GRAu substrates. Due to post annealing, bigger size dumbbell shaped Au NPs were formed preferentially at the defect sites followed by dewetting behavior of Au on the graphene layer. Depending on the density and size of Au NPs at these sites, ZnO NRs and NWs are formed.[22]

3.7. XPS Analysis. XPS measurement was carried out to confirm the Au functionalization at defect sites in graphene. Parts c and d of Figure 8 represent the high resolution core level C-1s XPS spectra in GR and GRAu samples, respectively. Figure 8e represents the core level Au-4f spectra in the GRAu sample. The spectrum shown in Figure 8c is deconvoluted into four bands. The band at 284.76 eV corresponds to the C═C (sp^2) bond arising from in-plane stretching of carbon atoms on the graphene surface, and the C—C band at 285.08 eV is attributed mostly to the sp^3 defects such as vacancies and point defects and substitutional atoms,[38] consistent with the Raman spectra discussed earlier. The bands at 288.06 and 290.45 eV are due to the partial epoxy (C—O—C) and carboxylic (COOH) functional groups attached to graphene, and the peak at 293.26 eV is attributed to sp^2-hybridized carbon atoms due to the π–π^* shake up features.[39] After surface modification with Au, the XPS spectra show an upshift in the binding energy and broadening of both sp^2 and sp^3 bands. The changes in the peak parameters obtained from the fitting are summarized in Table 1. The shift in binding energy is due to the change in the Fermi level of graphene after Au functionalization.[40] This is consistent with the Raman analysis that showed a shift in the G and 2D bands in GRAu. XPS analysis also revealed an increase in the fwhm of sp^2 and sp^3 bands by 0.15 and 0.55 eV, respectively, which may be due to the longer Au—C bonds caused by the covalent functionalization initiated at defect sites on graphene.[40] Interestingly, the ratio of integrated intensity of the sp^3 to sp^2 band calculated from Gaussian line shape fitting was found to be 40% lower in GRAu as compared to that in GR, strongly indicating covalent functionalization of graphene at the defect sites with Au and enhancement (reduction) in the sp^2 (sp^3) band, as evident from the data presented in Table 1. Note that the line width of the C—O—C band is more than double that of the C═C (sp^2) band, which indicates an attachment of native oxygenated functionalities on the graphene layer over the sp^3 sites during the room temperature storage. The Au-4f bands show an additional two Gaussian peaks at binding energies of 85.08 and 89.36 eV (Figure 8e) that may be due to the nominal oxidation of the Au NP surface. These results clearly establish the physical functionalization of GR with Au due to the presence of in-plane defects and are fully consistent with the Raman and HRTEM analyses. The upshift in Raman peak position and large broadening of the 2D band in GRAu are due to the change in electronic structure of the graphene after Au functionalization.

Table 1. Fitting Parameters of the C-1s Core Level XPS Spectra of GR and GRAu[a]

GR				GRAu		
band	peak	fwhm	I_{GR}	peak	fwhm	I_{GRAu}
C═C (sp^2)	284.76	1.19	28 067	284.82	1.34	36 380
C—C (sp^3)	285.08	2.09	42 046	285.42	2.64	39 008
C—O—C	288.06	3.25	14 233	288.2	2.88	9940
π—π^*	293.26	1.18	2298	293.41	2.32	4497

[a]Peak position and fwhm are in eV units. I_{GR} and I_{GRAu} represent integrated intensities of the corresponding bands in GR and GRAu, respectively.

3.8. Position Dependent Raman Profile. We further looked into the spatial uniformity and Au clustering through defect sites in GRAu by quantifying the defect density from the Raman intensity profile of the D and G bands. If we assume that the SPR effect caused equal intensity enhancement in both the D and G bands such that the intensity ratio remained unaffected, such an intensity ratio (I_D/I_G) can be used to the estimate the average interdefect distance (L_D) and defect density (n_D).[41] Figure 9a represents a set of Raman spectra scanned at the different positions of GRAu, as shown in the OM image of Figure 9b. Each spectrum was monitored by the position of scanned area where the areal densitiy of Au NPs is expected to be proportional to the areal density of defects. These spectra were taken on GRAu substrate under identical conditions. In order to calculate the n_D and L_D for a measured I_D/I_G ratio, we have used the empirical relations presented by Cancado et al.[41] These empirical relations were proposed with ~30% error based on the I_D/I_G values obtained in Raman spectra of Ar+ ion bombarded graphene with point defects separated by L_D > 10 nm and at visible excitation wavelengths.

$$L_D^{\,2}\ (\mathrm{nm}^2) = (1.8 \pm 0.5) \times 10^{-9} \lambda_L^{\,4} \left(\frac{I_D}{I_G}\right)^{-1} \quad (1)$$

$$n_D\ (\mu\mathrm{m}^{-2}) = \frac{(1.8 \pm 0.5)}{\lambda_L^{\,4}} \times 10^{14} \left(\frac{I_D}{I_G}\right) \quad (2)$$

dx.doi.org/10.1021/jp500501e | J. Phys. Chem. C 2014, 118, 13833–13843

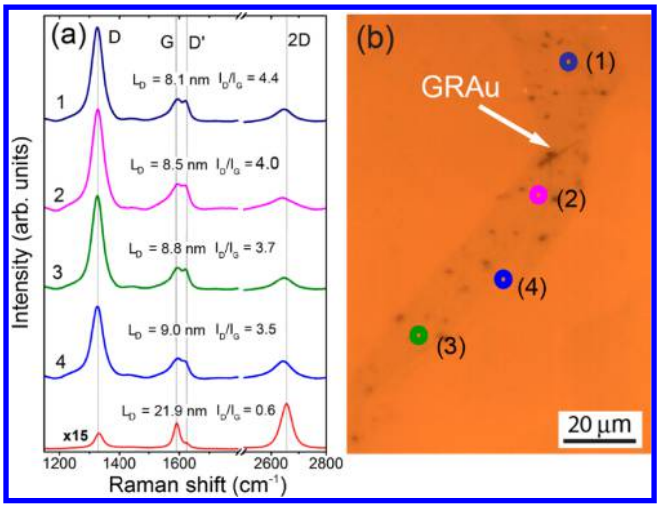

Figure 9. (a) Position dependent Raman profiles of GRAu and GR measured with λ_{ex} = 632.8 nm. Interdefect distance (L_D) values at each position were calculated from the I_D/I_G ratio using eq 1. Note that the spectrum for the pristine GR shown at the bottom is scaled up by a factor of 15 for comparison. (b) Corresponding OM image of scanning positions.

where λ_L is the excitation wavelength in nm. Using these empirical relations, the calculated L_D varies in the range 8.1−9.0 nm and n_D varies in the range 3985−4950 μm^{-2} for GRAu. On the other hand, pristine GR shows an L_D value of 21.9 nm and corresponding n_D value of 673 μm^{-2}. This implies a 6−7-fold increase in n_D after Au deposition on GR. Interestingly, manual counting of the point defects in the HRTEM image of GR and GRAu shown in Figure 3b and d reveals also a nearly 6-fold increase in the defect density after Au deposition. Thus, despite the large error bars involved in the empirical formula of eq 2, the Raman results are in close agreement with the HRTEM image analysis. Further, we have measured the average distance between centers of neighboring Au NPs at several positions in the HRTEM image. Interestingly, it is found that the average distance between two Au NPs is ∼7 nm (see Figure 6a), which is very close to the value of 8−9 nm calculated from the Raman analysis. Note that Raman analysis of the defect density is limited to the defects that are Raman active and gives rise to the D band. It has been found that perfect zigzag edges, charged impurities, intercalants, and uniaxial and biaxial strain in graphene do not generate a D band.[16] Thus, Raman analysis based on D band intensity may underestimate the defect density. However, in the above analysis, we have neglected any additional enhancement of the D band due to the local SPR effect of the Au NPs as compared to the SPR effect on the other bands. Thus, these two competing effects taken together make the result of Raman analysis fully consistent with HRTEM analysis. Further analysis of the spectra shown for four different positions (Figure 9a) reveals that there is no significant shift in peak position and change in fwhm of D, G, D′, and 2D bands for different locations of the GRAu sample scanned. Since the scanned area covers several square micrometers, any local nonuniformity in the nanometer scale is not reflected in the Raman data. Thus, the GRAu sample can be assumed to have good spatial homogeneity. A small downshift in the 2D peak position may be arising from local charged impurity present in the GRAu hybrid due to functionalization with Au atoms.[8]

A comparison of the fwhm of different Raman bands in GR and GRAu samples indicates that the fwhm of 2D and G bands are nearly doubled in GRAu as compared to that of GR. On the other hand, the fwhm of D and D′ bands do not change significantly despite a large change in intensity (see the Supporting Information, Figure S6). This indicates that D and D′ bands are resonantly enhanced due to the SPR effect at the defect sites of functionalized GRAu without losing the sp^2 crystalline nature of graphene. Note that the asymmetry and broadening of the G and 2D bands are due to the change in the electronic structure of graphene owing to Au interaction.

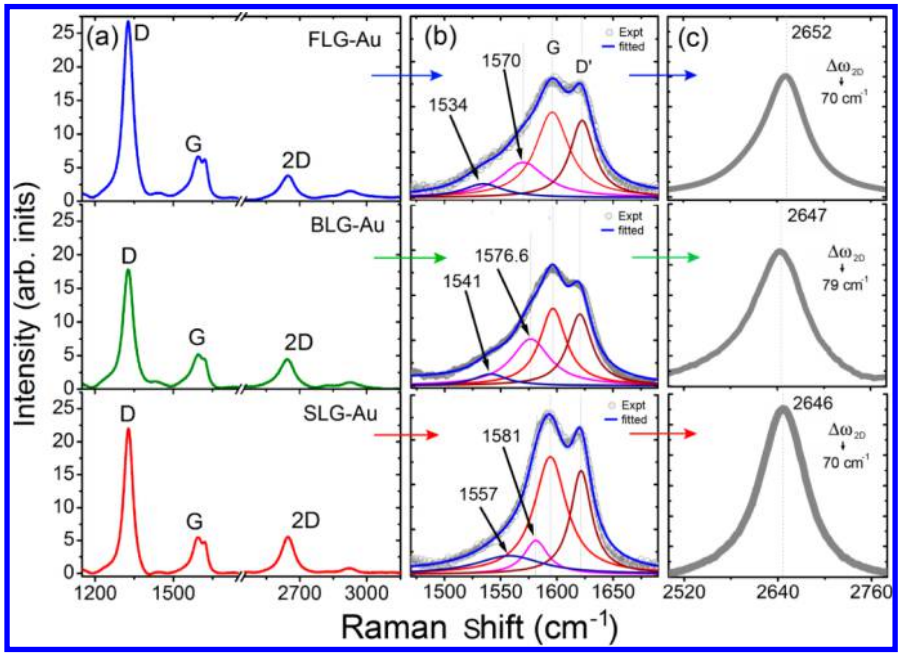

Figure 10. Comparison of Raman spectra for SLG, BLG, and FLG after Au deposition: (a) D, G, and 2D bands. (b) Lorentzian line shape fitting of G, D′, and additional low frequency modes marked in cm^{-1} units. (c) 2D band, peak position, and fwhm ($\Delta\omega_{2D}$) marked in cm^{-1} units in each case.

dx.doi.org/10.1021/jp500501e | J. Phys. Chem. C 2014, 118, 13833−13843

3.9. Effect of Number of Graphene Layers. The effect of the number of layers in graphene on the Au functionalization was further studied by line shape analysis of the Raman spectra. Figure 10a represents the Raman features of GRAu for single layer, bi layer, and few layer graphene (FLG). From the deconvolution of the G band using Lorentzian line shapes, as shown in Figure 10b and c, no shifts in G (1596 cm^{-1}) and D′ (1620 cm^{-1}) bands were observed. Interestingly, the fwhm of the 2D band in Au coated SLG and pristine BLG shows nearly identical values of ∼70 cm^{-1} (see Figure 2b). Thus, the Au coated SLG behaves like a pristine BLG where interaction between the Au and SLG layers may be as significant as that between the two layers of graphene in a BLG. This is an important observation, and it signifies the strong interaction between the Au and defective graphene layers.

Besides the common modes, additional Raman modes at 1581, 1576.6, and 1570 cm^{-1} were observed in SLG, BLG, and FLG, respectively, after Au deposition, which may be due to the covalent functionalization of Au at the defect sites.[40] A systematic downshift in the additional bands was observed as the number of graphene layers increased. The lower frequency peaks at ∼1557, 1541, and 1534 cm^{-1} may be resulting from the strain caused by the formation of Au−C bonds creating lattice distortions on the surrounding in-plane C−C stretching bonds of sp^2 carbon atoms, as discussed with reference to Figure 6c.[42] A weak feature at ∼1440 cm^{-1} next to the D band in Figure 10a arises probably from the sp^3 C contribution in the functionalized GRAu. In the case of BLG−Au, the intensity of the D band is marginally lower, which may be due to the interlayer interaction in graphene.

Note that, despite the chemically inert nature of the perfect graphene and Au atoms, defects in graphene cause strong interaction with Au atoms, leading to physical functionalization of GR. Such Au functionalized graphene may be highly desirable for binding of graphene with other functional molecules for biosensing and bioimaging applications. The functionalized graphene may be useful as a nanocarrier and find applications for drug delivery and related applications. Note that the strength of the interaction of Au and GR is expected to be proportional to the initial defect density and nature of defects in GR. However, there would be a limitation on graphene−foreign material interaction with respect to the areal density of defects without losing the sp^2 crystalline nature of graphene. Further, control of the defect density during the growth and by postgrowth processing will provide the additional handle or the practical use of the concept demonstrated here. More studies are underway to shed further light on this issue.

4. CONCLUSION

In conclusion, we have demonstrated in-plane defect mediated enhanced interaction of Au atoms with a graphene layer grown by the CVD method. Our Raman studies in conjunction with HRTEM imaging provide direct evidence of defect enhanced strong interaction of Au with the defect sites in graphene and physical functionalization of graphene at room temperature. A local SPR effect at the graphene−Au interface was identified from a strong enhancement of the D and D′ Raman modes and enhancement of the SPR peak in the absorption spectra. Raman mapping, AFM, and HRTEM analyses provided evidence for bonding of Au NPs at the defect sites in graphene. The interdefect distance and areal defect density calculated from the Raman analysis on GRAu are in close agreement with HRTEM analysis. These conclusions were further substantiated by the XPS analysis. Raman line shape analysis further suggested that ultrathin Au coated SLG behaves like a pristine BLG layer, lending support for strong interaction between the Au and the graphene layer. Our results open up possibilities for further study on defect engineering in graphene appropriate for physical functionalization of graphene with foreign atoms/molecules to accomplish new functionalities in graphene based hybrid structures. Our results also have important bearings on the development of graphene based junction devices and hybrid catalysts.

■ ASSOCIATED CONTENT

Ⓢ Supporting Information

Figure S1: Raman fingerprints of graphene before and after H_2 annealing and corresponding optical microscope images. Figure S2: Raman spectrum showing D and G band features in chemically processed graphene sheets and the corresponding TEM image along with the SAED pattern. Figure S3: FESEM images of GR and GRAu on SiO_2 substrate and TEM images of GRAu showing the Au NPs on graphene. Figure S4: Comparative Raman spectra of GR and GRCoPc. Figure S5: Absorption spectra of GRAu and GRCu. Figure S6: fwhm of D, D′, G, and 2D bands as a function of interdefect distance (L_D) in GR and GRAu. This material is available free of charge via the Internet at http://pubs.acs.org.

■ AUTHOR INFORMATION

Corresponding Author

*E-mail: giri@iitg.ernet.in. Phone: +91 361 2582703.

Notes

The authors declare no competing financial interest.

■ ACKNOWLEDGMENTS

We acknowledge Central Instrument Facility, IIT Guwahati, for providing micro-Raman and FESEM facilities. We acknowledge DST (No SR/55/NM−01/2005), Government of India, for supporting the HRTEM facility at IIT Guwahati. This work was partly supported by funding from BRNS and CSIR. P.K.G. acknowledges the JSPS invitation fellowship for long term research in Japan. We are grateful to Dr. K. Imakita for his help in the XPS measurement. We thank A. K. Sivadasan, Indira Gandhi Centre for Atomic Research (IGCAR), Kalpakkam, for his help in executing the Raman mapping measurements. R.K.B. expresses his gratitude to I. Talukdar for his constant support in HRTEM measurements. Thanks are due to V. V. N. Subbarao, Dr. S. Sharma, and Dr. S. Dhara, Kobe University, and Dr. S. Dhara, IGCAR, for their valuable suggestions.

■ REFERENCES

(1) Geim, A. K. Graphene: Status and Prospects. *Science* **2009**, *324* (5934), 1530−1534.

(2) Geim, A. K.; Novoselov, K. S. The rise of graphene. *Nat. Mater.* **2007**, *6* (3), 183−191.

(3) Nair, R. R.; Blake, P.; Grigorenko, A. N.; Novoselov, K. S.; Booth, T. J.; Stauber, T.; Peres, N. M. R.; K.Geim, A. Fine Structure Constant Defines Visual Transparency of Graphene. *Science* **2008**, *320* (5881), 1308.

(4) Ghosh, S.; Calizo, I.; Teweldebrhan, D.; Pokatilov, E. P.; Nika, D. L.; Balandin, A. A.; Bao, W.; Miao, F.; Lau, C. N. Extremely high thermal conductivity of graphene: Prospects for thermal management applications in nanoelectronic circuits. *Appl. Phys. Lett.* **2008**, *92* (15), 151911-3.

(5) Reckinger, N.; Vlad, A.; Melinte, S.; Colomer, J.-F.; Sarrazin, M. Graphene-coated holey metal films: Tunable molecular sensing by surface plasmon resonance. *Appl. Phys. Lett.* **2013**, *102* (21), 211108-4.
(6) Zhang, S. G.; Zhang, X. W.; Si, F. T.; Dong, J. J.; W, J. X.; et al. Ordered ZnO nanorods-based heterojunction light-emitting diodes with graphene current spreading layer. *Appl. Phys. Lett.* **2012**, *101*, 121104.
(7) Ding, M.; Tang, Y.; Star, A. Understanding Interfaces in Metal–Graphitic Hybrid Nanostructures. *J. Phys. Chem. Lett.* **2012**, *4* (1), 147–160.
(8) Bratescu, M. A.; Saito, N. Charge Doping of Large-Area Graphene by Gold-Alloy Nanoparticles. *J. Phys. Chem. C* **2013**, *117* (50), 26804–26810.
(9) Gong, W.; Zhang, W.; Ren, C.; Ke, X.; Wang, S.; Huai, P.; Zhang, W.; Zhu, Z. Strain-controlled interface engineering of binding and charge doping at metal-graphene contacts. *Appl. Phys. Lett.* **2013**, *103* (14), 143107-4.
(10) Yan, L.; Zheng, Y. B.; Zhao, F.; Li, S.; Gao, X.; Xu, B.; Weiss, P. S.; Zhao, Y. Chemistry and physics of a single atomic layer: strategies and challenges for functionalization of graphene and graphene-based materials. *Chem. Soc. Rev.* **2012**, *41* (1), 97–114.
(11) Bisquert, J. Nano-Enabled Photovoltaics. Progress in Materials and Methodologies. *J. Phys. Chem. Lett.* **2013**, *4* (6), 1051–1052.
(12) Gan, Y.; Sun, L.; Banhart, F. One- and Two-Dimensional Diffusion of Metal Atoms in Graphene. *Small* **2008**, *4* (5), 587–591.
(13) Urich, A.; Pospischil, A.; Furchi, M. M.; Dietze, D.; Unterrainer, K.; Mueller, T. Silver nanoisland enhanced Raman interaction in graphene. *Appl. Phys. Lett.* **2012**, *101* (15), 153113-4.
(14) Ramasse, Q. M.; Zan, R.; Bangert, U.; Boukhvalov, D. W.; Son, Y.-W.; Novoselov, K. S. Direct Experimental Evidence of Metal-Mediated Etching of Suspended Graphene. *ACS Nano* **2012**, *6* (5), 4063–4071.
(15) Lee, J.; Novoselov, K. S.; Shin, H. S. Interaction between Metal and Graphene: Dependence on the Layer Number of Graphene. *ACS Nano* **2010**, *5* (1), 608–612.
(16) Sarkar, S.; Moser, M. L.; Tian, X.; Zhang, X.; Al-Hadeethi, Y. F.; Haddon, R. C. Metals on Graphene and Carbon Nanotube Surfaces: From Mobile Atoms to Atomtronics to Bulk Metals to Clusters and Catalysts. *Chem. Mater.* **2013**, *26* (1), 184–195.
(17) Zan, R.; Bangert, U.; Ramasse, Q.; Novoselov, K. S. Metal–Graphene Interaction Studied via Atomic Resolution Scanning Transmission Electron Microscopy. *Nano Lett.* **2011**, *11* (3), 1087–1092.
(18) Wang, H.; Li, K.; Cheng, Y.; Wang, Q.; Yao, Y.; Schwingenschlogl, U.; Zhang, X.; Yang, W. Interaction between single gold atom and the graphene edge: A study via aberration-corrected transmission electron microscopy. *Nanoscale* **2012**, *4* (9), 2920–2925.
(19) Schedin, F.; Lidorikis, E.; Lombardo, A.; Kravets, V. G.; Geim, A. K.; Grigorenko, A. N.; Novoselov, K. S.; Ferrari, A. C. Surface-Enhanced Raman Spectroscopy of Graphene. *ACS Nano* **2010**, *4* (10), 5626.
(20) Wang, P.; Zhang, D.; Zhang, L.; Fang, Y. The SERS study of graphene deposited by gold nanoparticles with 785 nm excitation. *Chem. Phys. Lett.* **2013**, *556* (0), 146–150.
(21) Park, W.-H.; Jung, M.; Moon, J.-S.; Noh, S. H.; Kim, T. H.; Joo, M. H.; Park, K. H. Experimental identification of the out-of-plane phonon mode of a few layered graphene from individual Au nanoparticle-Au film junctions. *Appl. Phys. Lett.* **2013**, *103* (7), 071903-4.
(22) Biroju, R. K.; Giri, P. K.; Dhara, S.; Imakita, K.; Fujii, M. Graphene-Assisted Controlled Growth of Highly Aligned ZnO Nanorods and Nanoribbons: Growth Mechanism and Photoluminescence Properties. *ACS Appl. Mater. Interfaces* **2013**, *6* (1), 377–387.
(23) Xuesong Li, W. C.; An, J.; Kim, S.; Nah, J.; Yang, D.; Piner, R.; Velamakanni, A.; Jung, I.; Ruoff, R. S. Large Area synthesis of High-Quality Graphene Films on Copper Foils. *Science* **2009**, *324*, 1312–1314.
(24) Lin, Y.-C.; Lu, C.-C.; Yeh, C.-H.; Jin, C.; Suenaga, K.; Chiu, P.-W. Graphene Annealing: How Clean Can It Be? *Nano Lett.* **2011**, *12* (1), 414–419.
(25) Jorio, A.; Saito, R.; Dresselhaus, G.; Dresselhaus, M. S. *Raman Spectroscopy in Graphene Related Systems*, 1st ed.; Wiley VCH Verlag GmbH & Co. KGaA: Weinheim, Germany, 2009.
(26) Dresselhaus, M. S.; Jorio, A.; Hofmann, M.; Dresselhaus, G.; Saito, R. Perspectives on Carbon Nanotubes and Graphene Raman Spectroscopy. *Nano Lett.* **2010**, *10* (3), 751–758.
(27) Malard, L. M.; Pimenta, M. A.; Dresselhaus, G.; Dresselhaus, M. S. Raman spectroscopy in graphene. *Phys. Rep.* **2009**, *473* (5–6), 51–87.
(28) Ferrari, A. C.; Basko, D. M. Raman spectroscopy as a versatile tool for studying the properties of graphene. *Nat. Nanotechnol.* **2013**, *8* (4), 235–246.
(29) Lucchese, M. M.; Stavale, F.; Ferreira, E. H. M.; Vilani, C.; Moutinho, M. V. O.; Capaz, R. B.; Achete, C. A.; Jorio, A. Quantifying ion-induced defects and Raman relaxation length in graphene. *Carbon* **2010**, *48* (5), 1592–1597.
(30) Subrahmanyam, K. S.; Manna, A. K.; Pati, S. K.; Rao, C. N. R. A study of graphene decorated with metal nanoparticles. *Chem. Phys. Lett.* **2010**, *497*, 70–75.
(31) Yoo, E.; Okata, T.; Akita, T.; Kohyama, M.; Nakamura, J.; Honma, I. Enhanced Electrocatalytic Activity of Pt Subnanoclusters on Graphene Nanosheet Surface. *Nano Lett.* **2009**, *9* (6), 2255–2259.
(32) Zhou, M.; Zhang, A.; Dai, Z.; Zhang, C.; Feng, Y. P. Greatly enhanced adsorption and catalytic activity of Au and Pt clusters on defective graphene. *J. Chem. Phys.* **2010**, *132* (19), 194704.
(33) Cretu, O.; Krasheninnikov, A. V.; Rodríguez-Manzo, J. A.; Sun, L.; Nieminen, R. M.; Banhart, F. Migration and Localization of Metal Atoms on Strained Graphene. *Phys. Rev. Lett.* **2010**, *105* (19), 196102.
(34) Logsdail, A. J.; Akola, J. Interaction of Au16 Nanocluster with Defects in Supporting Graphite: A Density-Functional Study. *J. Phys. Chem. C* **2011**, *115* (31), 15240–15250.
(35) Cong, C.; Yu, T.; Saito, R.; Dresselhaus, G. S.; Dresselhaus, M. S. Second-Order Overtone and Combination Raman Modes of Graphene Layers in the Range of 1690–2150 cm-1. *ACS Nano* **2011**, *5* (3), 1600–1605.
(36) Rao, R.; Podila, R.; Tsuchikawa, R.; Katoch, J.; Tishler, D.; Rao, A. M.; Ishigami, M. Effects of Layer Stacking on the Combination Raman Modes in Graphene. *ACS Nano* **2011**, *5* (3), 1594–1599.
(37) Wang, H.; Feng, Q.; Cheng, Y.; Yao, Y.; Wang, Q.; Li, K.; Schwingenschlögl, U.; Zhang, X. X.; Yang, W. Atomic Bonding between Metal and Graphene. *J. Phys. Chem. C* **2013**, *117* (9), 4632–4638.
(38) Eckmann, A.; Felten, A.; Mishchenko, A.; Britnell, L.; Krupke, R.; Novoselov, K. S.; Casiraghi, C. Probing the Nature of Defects in Graphene by Raman Spectroscopy. *Nano Lett.* **2012**, *12* (8), 3925–3930.
(39) Skaltsas, T.; Ke, X.; Bittencourt, C.; Tagmatarchis, N. Ultrasonication Induces Oxygenated Species and Defects onto Exfoliated Graphene. *J. Phys. Chem. C* **2013**, *117* (44), 23272–23278.
(40) Kim, Y. A.; Fujisawa, K.; Muramatsu, H.; Hayashi, T.; Endo, M.; Fujimori, T.; Kaneko, K.; Terrones, M.; Behrends, J.; Eckmann, A.; Casiraghi, C.; Novoselov, K. S.; Saito, R.; Dresselhaus, M. Raman Spectroscopy of Boron-Doped Single-Layer Graphene. *ACS Nano* **2012**, *6* (7), 6293–6300.
(41) Cançado, L. G.; Jorio, A.; Ferreira, E. H. M.; Stavale, F.; Achete, C. A.; Capaz, R. B.; Moutinho, M. V. O.; Lombardo, A.; Kulmala, T. S.; Ferrari, A. C. Quantifying Defects in Graphene via Raman Spectroscopy at Different Excitation Energies. *Nano Lett.* **2011**, *11* (8), 3190–3196.
(42) Huanga, M.; Yanb, H.; Chena, C.; Songb, D.; Heinzb, T. F.; Honea, J. Phonon softening and crystallographic orientation of strained graphene studied by Raman spectroscopy. *Proc. Natl. Acad. Sci. U.S.A.* **2009**, *106* (18), 7304–7308.